

Article

# Storage of Lithium-Ion by Phase Engineered MoO<sub>3</sub> Homojunctions

Dickon H. L. Ng<sup>1,\*†</sup>, Sheng Li<sup>2,†</sup>, Jun Li<sup>2</sup>, Jinning Huang<sup>3</sup>, Yingxue Cui<sup>2</sup>, Jiabiao Lian<sup>2</sup> and Chuan Wang<sup>3,\*</sup>

<sup>1</sup> School of Science and Engineering, The Chinese University of Hong Kong (Shenzhen), Longgang, Shenzhen 518172, China

<sup>2</sup> Key Laboratory of Zhenjiang, Institute for Energy Research, Jiangsu University, Zhenjiang 212013, China

<sup>3</sup> Institute of Advanced Synthesis, School of Chemistry and Molecular Engineering, Jiangsu National Synergetic Innovation Center for Advanced Materials, Nanjing Tech University, 30 Puzhu South Road, Nanjing 211800, China

\* Correspondence: dickonng@cuhk.edu.cn (D.H.L.N.); ias\_cwang@njtech.edu.cn (C.W.)

† These authors contributed equally to this work.

**Abstract:** With high theoretical specific capacity, the low-cost MoO<sub>3</sub> is known to be a promising anode for lithium-ion batteries. However, low electronic conductivity and sluggish reaction kinetics have limited its ability for lithium ion storage. To improve this, the phase engineering approach is used to fabricate orthorhombic/monoclinic MoO<sub>3</sub> ( $\alpha$ /h-MoO<sub>3</sub>) homojunctions. The  $\alpha$ /h-MoO<sub>3</sub> is found to have excessive hetero-phase interface. This not only creates more active sites in the MoO<sub>3</sub> for Li<sup>+</sup> storage, it regulates local coordination environment and electronic structure, thus inducing a built-in electric field for boosting electron/ion transport. In using  $\alpha$ /h-MoO<sub>3</sub>, higher capacity (1094 mAh g<sup>-1</sup> at 0.1 A g<sup>-1</sup>) and rate performance (406 mAh g<sup>-1</sup> at 5.0 A g<sup>-1</sup>) are obtained than when using only the single phase h-MoO<sub>3</sub> or  $\alpha$ -MoO<sub>3</sub>. This work provides an option to use  $\alpha$ /h-MoO<sub>3</sub> hetero-phase homojunction in LIBs.

**Keywords:** anode materials; phase engineering; molybdenum trioxide; homojunctions; lithium-ion storage



**Citation:** Ng, D.H.L.; Li, S.; Li, J.; Huang, J.; Cui, Y.; Lian, J.; Wang, C. Storage of Lithium-Ion by Phase Engineered MoO<sub>3</sub> Homojunctions. *Nanomaterials* **2022**, *12*, 3762. <https://doi.org/10.3390/nano12213762>

Academic Editor: Carlos Miguel Costa

Received: 18 September 2022

Accepted: 24 October 2022

Published: 26 October 2022

**Publisher's Note:** MDPI stays neutral with regard to jurisdictional claims in published maps and institutional affiliations.



**Copyright:** © 2022 by the authors. Licensee MDPI, Basel, Switzerland. This article is an open access article distributed under the terms and conditions of the Creative Commons Attribution (CC BY) license (<https://creativecommons.org/licenses/by/4.0/>).

## 1. Introduction

Owing to the high energy density, flexibility in design and long cyclic life, lithium-ion batteries (LIBs) are playing essential roles in our modern society, from domestic electronic products to electric vehicles (EVs) and aerospace carriers [1,2]. Nonetheless, current commercial graphite electrodes provide limited rate capacity and having sluggish Li<sup>+</sup> intercalation which are insufficient to meet the demands of the next generation of LIBs [3]. It is highly desirable to exploit new anode materials with higher rates to meet demands for various applications [4,5]. Among the commonly used transition metal oxides for anode materials, the low cost MoO<sub>3</sub> has relatively high theoretical specific capacity (1117 mA h g<sup>-1</sup>, much higher than commercial graphite (372 mA h g<sup>-1</sup>)) [6–9]. However, the Li<sup>+</sup> storage performance of MoO<sub>3</sub> is suppressed by the inherently low electronic conductivity, sluggish Li<sup>+</sup> diffusion kinetics and the large volume change, resulting in severe polarization and poor rate performance [10,11]. In the exploration aiming to enhance the kinetics of MoO<sub>3</sub>, some of the work involved the designing of nano/micro-architecture to increase the contact area with the electrolyte [12–14], incorporating a carbon-based conductive matrix to enhance the stability [15–17], and introducing defects to optimize conductivity [18,19]. To some extent, the above-mentioned strategies have improved structure stability and electrical conductivity, while the intrinsic slow ion migration property of MoO<sub>3</sub> remains and impedes the utilization of MoO<sub>3</sub> [20–22]. Thus, it is imperative to exploit universal strategies to boost the electrochemical performance of the MoO<sub>3</sub>. Fortunately, phase engineering is an effective and powerful strategy to modulate the physicochemical properties

and functionalities by tailoring transformation of different phases in nanomaterials [23–28]. In previous research, Song et al. studied cubic/orthorhombic-CoSe<sub>2</sub> homojunctions, and found that these heterojunctions would redistribute the interfacial charges and accelerated the ion diffusion, resulting in better performance of the sodium/potassium storage than those using cubic or orthorhombic CoSe<sub>2</sub> [29]. It is evident that the different crystallographic structure determines its unique electrochemical property. The MoO<sub>3</sub> usually exists in two structural phases, namely orthorhombic ( $\alpha$ -MoO<sub>3</sub>), and monoclinic (h-MoO<sub>3</sub>). It is highly feasible to make and use hetero-phase homojunctions for MoO<sub>3</sub> as electrode materials for electrochemical performance.

In this work, orthorhombic/monoclinic MoO<sub>3</sub> ( $\alpha$ /h-MoO<sub>3</sub>) homojunctions were fabricated via partial phase transformation with a facile heat treatment. Compared with heterojunctions, the homojunction with interfaces exhibit stronger electron coupling due to their similar physicochemical properties and lattice matching. At the unique homojunction interfaces, the unbalanced charge distribution would also create an internal electric field, which facilitates the interfacial charge transport, accelerates ion diffusion, increases the reactive sites and improves the electrochemical surface reaction kinetics. The work demonstrates that  $\alpha$ /h-MoO<sub>3</sub> electrodes could delivered an extraordinarily high capacity of 1094 mAh g<sup>-1</sup> at 100 mA g<sup>-1</sup> with outstanding cyclic stability and a capacity of 462 mAh g<sup>-1</sup> remaining after 300 cycles of operation at 1.0 A g<sup>-1</sup>. This work confirms that, via constructing the hetero-phase homojunction in MoO<sub>3</sub>, Li<sup>+</sup>, storage kinetics can be largely enhanced.

## 2. Materials and Methods

### 2.1. Material Preparation

The monoclinic (h-MoO<sub>3</sub>), orthorhombic/monoclinic MoO<sub>3</sub> ( $\alpha$ /h-MoO<sub>3</sub>) and orthorhombic MoO<sub>3</sub> ( $\alpha$ -MoO<sub>3</sub>) samples were prepared as follows. For synthesis of a typical sample, 2.0 g of Ammonium molybdate tetrahydrate ((NH<sub>4</sub>)<sub>6</sub>Mo<sub>7</sub>O<sub>24</sub>·4H<sub>2</sub>O) was dispersed into 10 mL deionized water before 1 mL HNO<sub>3</sub> was added into the solution under stirring for 30 min. The mixture was transferred to a 50 mL autoclave and heated at 180 °C for 12 h. The product was collected and washed with deionized water and ethanol before being dried in an oven at 60 °C overnight. This product was named Sample A. Subsequently, Sample A was heat-treated in a tube furnace at 400 °C for 30 min to produce Sample B. Thereafter, Sample B was further treated at 450 °C for 30 min to obtain Sample C.

### 2.2. Characterization

The composition and phase information of the samples were determined by X-ray diffractometry (XRD, Bruker D8, Mannheim, Germany). The morphology and microstructure of the samples were examined by the scanning electron microscope (SEM, JEOL, JSM-7800F, Tokyo, Japan). The Raman spectra were performed by using a DXR Raman system spectrometer (Thermo Scientific, Waltham, MA, USA) with a 532 nm laser.

### 2.3. Electrochemical Measurements

Cyclic voltammetry (CV) and electrochemical impedance spectroscopy (EIS) measurements were conducted on a Gamry (Interface 1000 E Potentiostat) electrochemical workstation. The galvanostatic discharge and charge profiles were measured by the NEWARE-CT-4008 battery tester. The working electrodes were prepared by mixing the MoO<sub>3</sub>, super conductive carbon black (SCCB, Ketjenblack EC-600JD, Lion Corporation, Tokyo, Japan) and polyvinylidene fluorid (PVDF) binder in N-methyl-2-pyrrolidone (NMP) with a weight ratio of 8:1:1. After stirring for 1 h, the homogeneous slurry was coated onto a copper foil. The mass loading of the active material was estimated to be about 1.0 mg cm<sup>-2</sup>. The CR2032 coin-type cells using the fabricated product were assembled in an argon-filled glovebox (oxygen/moisture concentrations < 0.01 ppm). Celgard 2400 porous polypropylene membrane was used as the separator. The electrolyte is 1 M LiPF<sub>6</sub> in carbonate (EC)/dimethyl carbonate (DMC) with the volume ratio of 1:1.

### 3. Results and Discussion

Powder X-ray diffractometry (XRD) and Raman scattering (RS) spectroscopy were used to investigate the phase structures and purity of MoO<sub>3</sub> with different phases. As shown in Figure 1a, the narrow and sharp diffraction peaks in the XRD patterns indicate the superior crystallinity of h-MoO<sub>3</sub> (Sample A),  $\alpha$ /h-MoO<sub>3</sub> (Sample B), and  $\alpha$ -MoO<sub>3</sub> (Sample C). The characteristic peaks at 9.6°, 19.4°, 25.7°, 29.3°, 35.4°, 45.5°, and 69° can be assigned to (100), (200), (210), (300), (310), (410), and (524) of hexagonal MoO<sub>3</sub> (PDF#21-0569) [27,30]. No other peaks are observed in the pattern of the h-MoO<sub>3</sub> (top of Figure 1a), indicating that there are no impurities. The middle pattern of  $\alpha$ /h-MoO<sub>3</sub> in Figure 1a contains new peaks at 12.8°, 23.2°, 25.5°, and 27.1°, which can be indexed to the (020), (110), (040), and (021) planes of  $\alpha$ -MoO<sub>3</sub>, respectively (PDF#35-0609) [15]. It is evident that h-MoO<sub>3</sub> under air atmosphere partially transfers to  $\alpha$ /h-MoO<sub>3</sub> at 400 °C. The subsequent heat treatment of  $\alpha$ /h-MoO<sub>3</sub> leads to the formation of thermodynamically stable  $\alpha$ -MoO<sub>3</sub> pillar at 450 °C as confirmed in the bottom pattern in Figure 1a. To better elucidate the crystal structures, Raman characterization was performed and the results are shown in Figure 1b. The signal peaks at 206 cm<sup>-1</sup>, 240 cm<sup>-1</sup>, 681 cm<sup>-1</sup>, 881 cm<sup>-1</sup>, and 969 cm<sup>-1</sup> are attributed to h-MoO<sub>3</sub> [24]. Meanwhile, the Raman spectrum of the  $\alpha$ -MoO<sub>3</sub> shows the characteristic bands at 148 cm<sup>-1</sup>, 235 cm<sup>-1</sup>, 281 cm<sup>-1</sup>, 328 cm<sup>-1</sup>, 658 cm<sup>-1</sup>, 813 cm<sup>-1</sup>, 813 cm<sup>-1</sup>, and 990 cm<sup>-1</sup> [15]. Notably, the Raman peaks correspond to  $\alpha$ /h-MoO<sub>3</sub> indicating that the hexagonal and orthorhombic crystal phases coexist, which is consistent with the XRD results (Figure 1a). The characterization results suggest the successful generation of homo-junctions in  $\alpha$ /h-MoO<sub>3</sub>, which is expected to synergize the benefits from different phases for improving the electrochemical performance.

The morphological characteristics of the MoO<sub>3</sub> samples were investigated by SEM. The homogeneous hexagonal crystals were clearly observed and shown in Figure 2. Figure 2a–c all show similar hexagonal prism morphology with a length of about 10  $\mu$ m, indicating their morphology was preserved during the heat treatment. In the high-magnification images (Figure 2d–f), an interesting conversion was observed. Compared to h-MoO<sub>3</sub>, the surface of  $\alpha$ /h-MoO<sub>3</sub> and  $\alpha$ -MoO<sub>3</sub> appears rough, which is attributed to the evolution of gases during heat treatment.

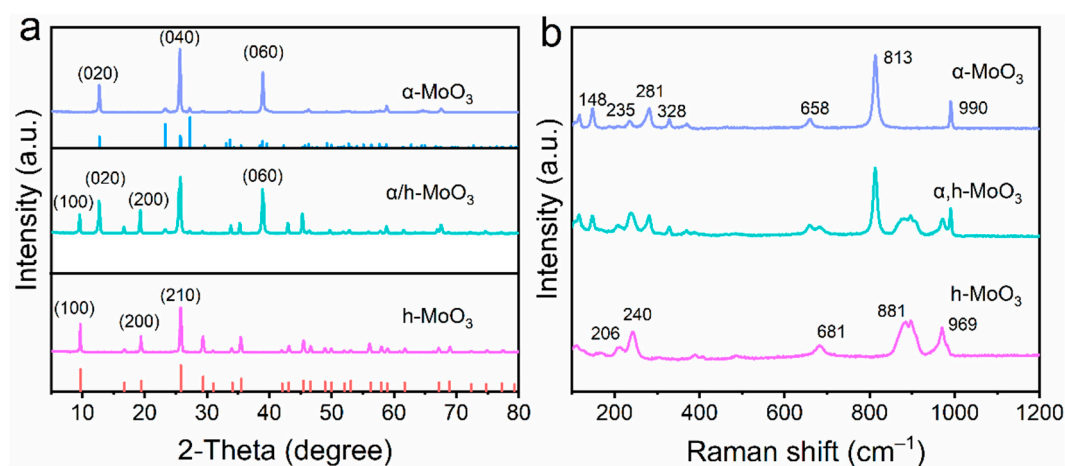


**Figure 1.** (a) XRD patterns and (b) Raman spectra of Sample A: h-MoO<sub>3</sub>, Sample B:  $\alpha$ /h-MoO<sub>3</sub>, and Sample C:  $\alpha$ -MoO<sub>3</sub>.

The Li<sup>+</sup> storage behavior of MoO<sub>3</sub> electrodes were systematically evaluated in a coin cell configuration in a potential window of 0.01 V to 3.0 V. Figure 3 shows the results of the electrochemical processes of  $\alpha$ /h-MoO<sub>3</sub>, h-MoO<sub>3</sub> and  $\alpha$ -MoO<sub>3</sub>. Their initial three cyclic voltammetry (CV) curves at a scan rate of 0.1 mV s<sup>-1</sup> are shown in Figure 3a–c, while their corresponding initial three GCD profiles are displayed in Figure 3d–f. It is noted that, in the first cathodic sweep, the irreversible reduction peak occurring at 2.6 V and

2.2 V could be assigned to the multistep  $\text{Li}^+$  insertion into  $\text{MoO}_3$  ( $\text{MoO}_3 + x\text{Li}^+ + xe^- \leftrightarrow \text{Li}_x\text{MoO}_3$ ); the irreversible peak at 0.7 V is due to the decomposition of electrolytes and the formation of the SEI layer, which disappears in the following cycles and thus causes part of the observed irreversible capacity during the first cycle [17]. On the other hand, a reduction peak at 0.17 V corresponds to the formation of Mo metal by conversion reaction ( $\text{Li}_x\text{MoO}_3 + (6 - x)\text{Li}^+ + (6 - x)e^- \leftrightarrow \text{Mo} + \text{Li}_2\text{O}$ ) [19].

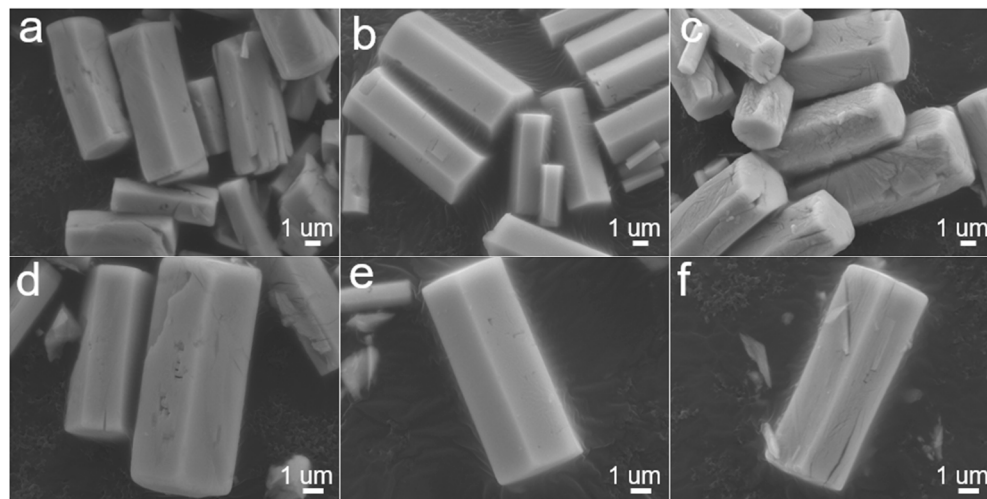


**Figure 2.** SEM images of (a,d) Sample B:  $\alpha/\text{h-MoO}_3$ , (b,e) Sample A:  $\text{h-MoO}_3$ , and (c,f) Sample C:  $\alpha\text{-MoO}_3$ , respectively.

In the anodic scans, the observed two oxidation peaks around 1.2 V, 1.7 V, and 2.6 V were attributed to the reversible reaction from Mo and  $\text{Li}_2\text{O}$  to  $\text{Li}_x\text{MoO}_3$  during delithiation process, respectively [31]. The second and third cathodic scans show the lithium intercalation at 1.6 V and the conversion reaction peak at 0.13 V, indicating an amorphous structure of  $\alpha/\text{h-MoO}_3$  is formed [15]. Meanwhile, the two CV curves almost overlapping suggests the good reversibility of the  $\alpha/\text{h-MoO}_3$  electrode during the repeated  $\text{Li}^+$  insertion and extraction. Compared to the CV profiles of  $\text{h-MoO}_3$  (Figure 3b), there are some differences, e.g., that the conversion reaction occurs at 0.37 V and one broad anodic peak at 1.4 V corresponds to the reversible  $\text{Li}^+$  extraction. The CV evolution of  $\alpha\text{-MoO}_3$  (Figure 3c) displays similar features to  $\alpha/\text{h-MoO}_3$ . Moreover, to highlight the different electrochemical behavior of these three electrodes, their first CV cycles were integrated in one image, as shown in Figure S1. Impressively, the initial three galvanostatic discharge-charge (GCD) profiles of the  $\alpha/\text{h-MoO}_3$ ,  $\text{h-MoO}_3$ , and  $\alpha\text{-MoO}_3$  electrodes at current density of  $0.1 \text{ A g}^{-1}$  is shown in Figure 3d–f, respectively, where the platforms agree well with the CV results (Figure 3a–c). The initial discharge and charge capacities were 1677 and 1091  $\text{mAh g}^{-1}$ , with an initial Coulombic efficiency of 65%. It is higher than  $\text{h-MoO}_3$  and  $\alpha\text{-MoO}_3$  (Figure 3e,f). The low initial coulombic efficiency might be caused by irreversible processes of SEI film and the capture of  $\text{Li}^+$  in the  $\text{MoO}_3$  lattice, which is also observed in initial CV cycles [32]. In successive charge–discharge cycles, it should be noticed that the GCD profiles of  $\alpha/\text{h-MoO}_3$  become stable with a coulombic efficiency of 95%, but the gradual capacity fade of  $\text{h-MoO}_3$  and  $\alpha\text{-MoO}_3$  is obvious. This suggests a good  $\text{Li}^+$  storage reversibility of the  $\alpha/\text{h-MoO}_3$  electrode, due to the orthorhombic/monoclinic homojunctions facilitating the reversible lithiation/delithiation process by increasing the electronic conductivity and mechanical integrity of the  $\text{MoO}_3$  electrode against structural changes. The rate and cycle performance comparison are presented in Figure 3g. The  $\alpha/\text{h-MoO}_3$  electrode displays reversible specific capacities 1094, 974, 846, 742, 562, and 406  $\text{mAh g}^{-1}$  with current densities increased from 0.1 to 0.25, 0.5, 1.0, 2.5, and 5.0  $\text{A g}^{-1}$ , respectively. As the current density regularly returns to 0.1  $\text{A g}^{-1}$ , the reversible capacity of 846  $\text{mAh g}^{-1}$  can still be obtained, suggesting good electrochemical reversibility. On the contrary, the  $\text{h-MoO}_3$

and  $\alpha$ -MoO<sub>3</sub> electrodes show a poorer rate of capability, resulting in lower capacities (125 and 222 mAh g<sup>-1</sup>) at high current density 5.0 A g<sup>-1</sup>. Figure S2 shows the corresponding galvanostatic charge–discharge (GCD) profiles for the  $\alpha$ /h-MoO<sub>3</sub>, h-MoO<sub>3</sub> and  $\alpha$ -MoO<sub>3</sub> electrodes at various current rates. It is obvious that the charge/discharge profiles of the  $\alpha$ /h-MoO<sub>3</sub> electrode displays much lower polarization at varied current densities [32], illustrating better reversible performance and less polarization at a high current. Therefore, it can be inferred that the homogenous orthorhombic/monoclinic interface with more Li storage active sites and enhanced electronic conductivity and Li<sup>+</sup> transport [33,34], resulting in high capacities and superior rate performance for the  $\alpha$ /h-MoO<sub>3</sub> electrode. Subsequently, the long-term cycling stabilities of different electrodes were examined at 1.0 A g<sup>-1</sup>. It is obvious that the  $\alpha$ /h-MoO<sub>3</sub> electrode delivered a reversible capacity of 462 mAh g<sup>-1</sup> over 300 cycles and satisfying capacity retention of 74%, which is higher than those of h-MoO<sub>3</sub> (339 mAh g<sup>-1</sup>) and  $\alpha$ -MoO<sub>3</sub> (409 mAh g<sup>-1</sup>). The above results evidentially demonstrate that the homojunctions effectively alleviate the pulverization and minimize the volume change to maintain structural integrity during the Li<sup>+</sup> insertion/extraction process [21].

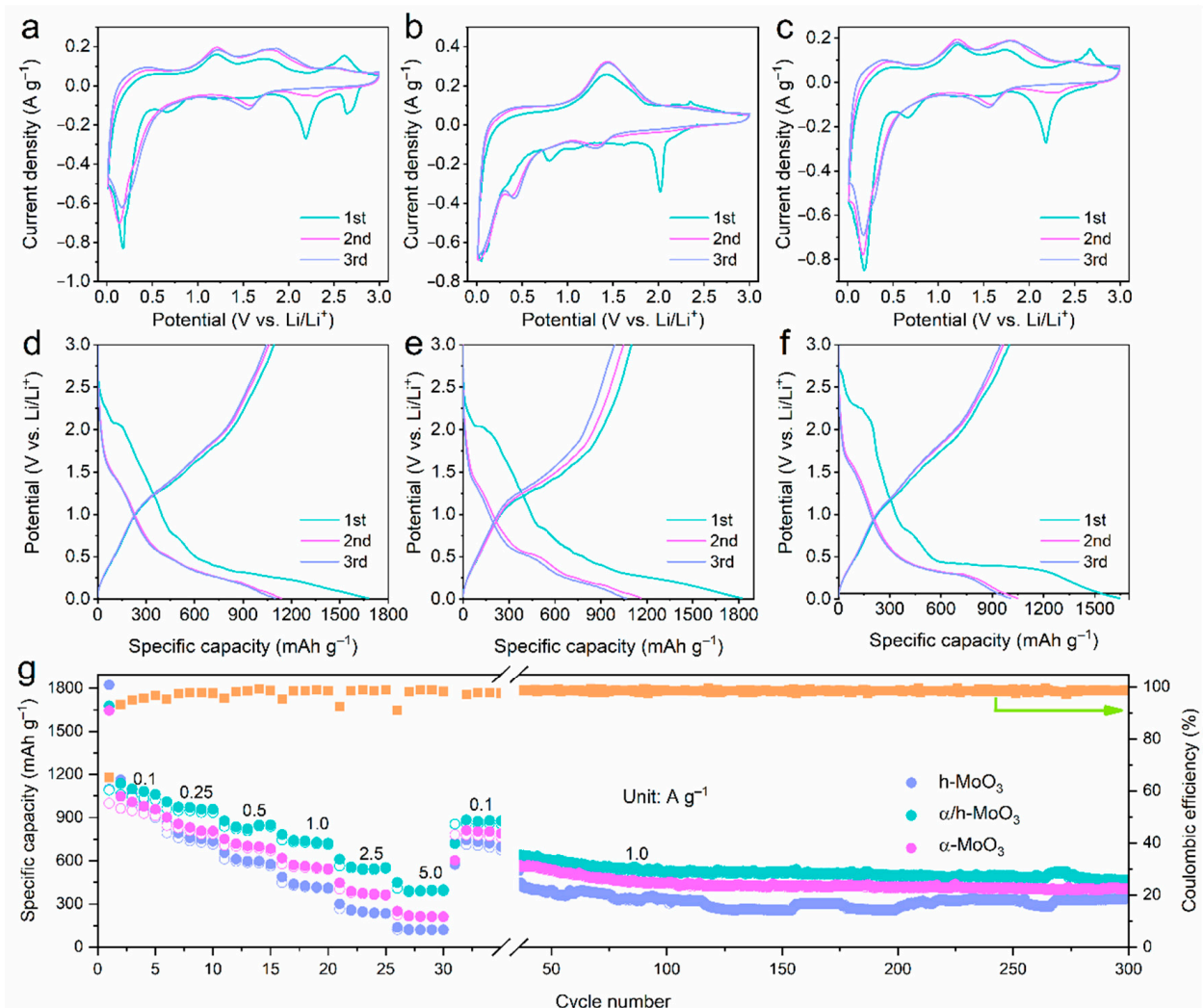


**Figure 3.** Electrochemical Li<sup>+</sup> storage performance of MoO<sub>3</sub> electrodes. The initial three CV curves at 0.1 mV s<sup>-1</sup> and GCD profiles at 0.1 A g<sup>-1</sup> of (a,d) Sample B:  $\alpha$ /h-MoO<sub>3</sub>; (b,e) Sample A: h-MoO<sub>3</sub>; (c,f) Sample C:  $\alpha$ -MoO<sub>3</sub>. (g) Rate capability and long-term cycling stability.

In order to have better understanding of the role of the homojunction structure for such enhanced rate capability of  $\alpha$ /h-MoO<sub>3</sub> electrodes, the CV curves at various scan rates of 0.1–5.0 mV s<sup>-1</sup> (Figure 4a,c,e) were conducted to investigate Li<sup>+</sup> storage kinetics.

In principle, the relationship between current  $i$  and scan rate  $v$  was investigated according to the following power law [35]:

$$i = av^b \quad (1)$$

$$\log(i) = b\log(v) + \log(a) \quad (2)$$

where  $i$  is peak current,  $v$  is sweep rate,  $a$  and  $b$  are adjustable values. When the  $b$ -Value closes to 0.5 indicating diffusion-controlled mechanism or 1.0 corresponding to capacitive-controlled process for  $\text{Li}^+$  storage behaviors, respectively. The corresponding fitted line for both cathodic and anodic peak currents can be found in Figure 4b,d,f. The  $b$  value of  $\alpha/\text{h-MoO}_3$ ,  $\text{h-MoO}_3$  and  $\alpha/\text{h-MoO}_3$  could be obtained as 0.73/0.68, 0.72/0.59, and 0.75/0.68 for cathodic/anodic peaks, respectively, implying that the  $\text{Li}^+$  storage kinetics was both dominated by surface capacitive behaviors and diffusion controlled. Figure 4g presents the electrochemical impedance spectrum (EIS) for further understanding of the  $\text{Li}^+$  diffusion kinetics and electrical resistance of three electrodes at open circuit potential. Generally, Nyquist plots are composed of three compositions: the intersection point on the real axis corresponds to the overall resistance of the cell components ( $R_s$ ), a semicircle at high frequency associated with the charge transfer resistance ( $R_{ct}$ ), and at low frequency line related to  $\text{Li}^+$  diffusion ( $Z_w$ ) [33]. It is apparent that the  $\alpha/\text{h-MoO}_3$  electrode shows smaller diameter and larger slope, suggesting lower charge-transfer resistance and faster  $\text{Li}^+$  diffusion in the electrode, guaranteeing a much better rate performance of the  $\alpha/\text{h-MoO}_3$  electrode. Meanwhile, the Warburg factor ( $\sigma$ ) was obtained from the plotting of  $Z'$  vs.  $\omega^{-1/2}$  (Figure 4i). It is noteworthy to mention that the slope of fitted lines of  $\alpha/\text{h-MoO}_3$  electrode is the smaller than that of the other electrodes, suggesting a better  $\text{Li}^+$  diffusion capacity. The above results illustrate that phase engineering is an effective and expandable mean to endow the electrode with fast electrochemical kinetics and a stable structure for superior  $\text{Li}^+$  storage.

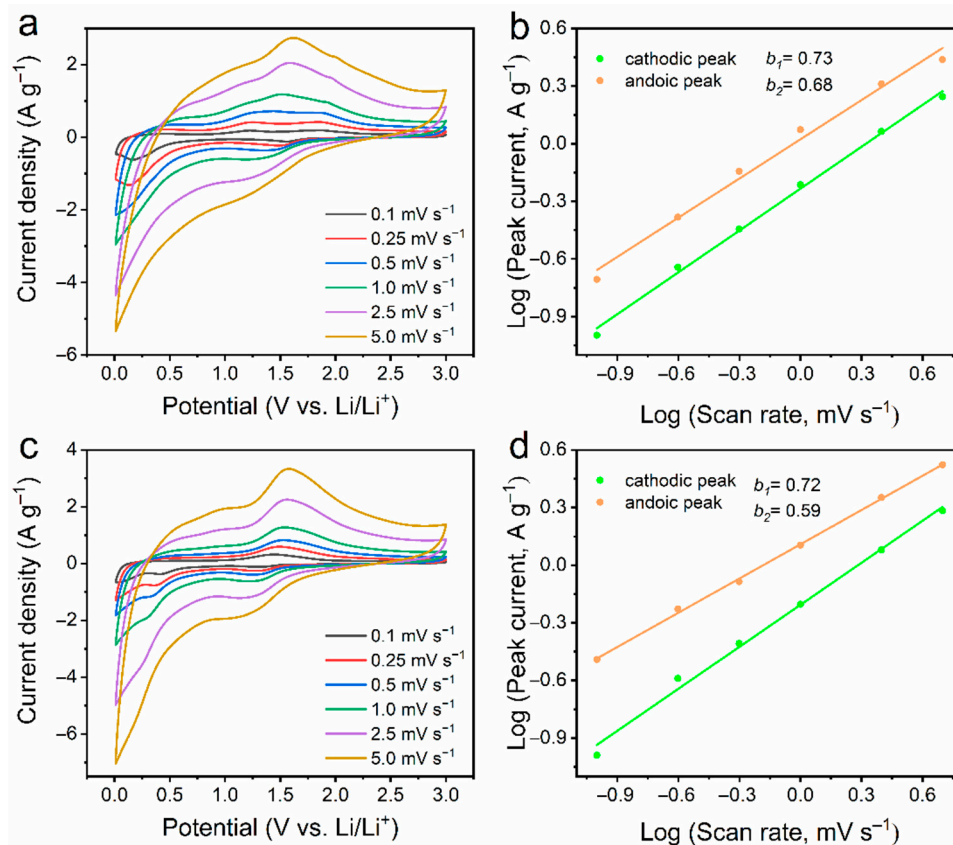
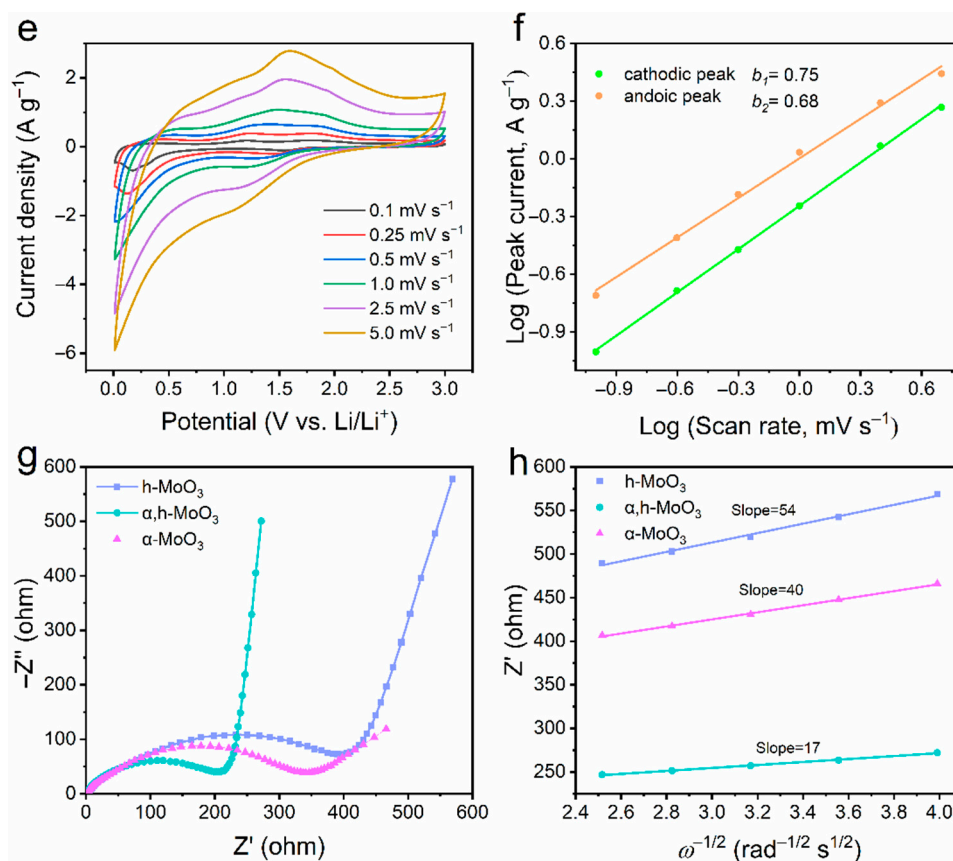


Figure 4. Cont.



**Figure 4.** The CV curves at different scan rates and corresponding  $b$ -value determinations of (a,b) Sample B:  $\alpha/h$ -MoO<sub>3</sub>, (c,d) Sample A: h-MoO<sub>3</sub>, and (e,f) Sample C:  $\alpha$ -MoO<sub>3</sub>. (g) Electrochemical impedance spectra and (h)  $Z' - \omega^{-1/2}$  plots.

#### 4. Conclusions

In summary, the  $\alpha/h$ -MoO<sub>3</sub> hetero-phase homojunction was prepared by a partial crystal phase transition. The product exhibited higher rate capability and better cyclic stability. The homojunctions not only showed the enhanced electronic conductivity and Li<sup>+</sup> diffusion, but also provided more intrinsic active sites and accommodate the volume expansion during discharge/charge. All these simultaneously enhanced the charge storage capability for higher capacity and superior rate performance. Benefiting from these merits, the  $\alpha/h$ -MoO<sub>3</sub> electrode delivered superior electrochemical performance. Specifically, an excellent rate ability (742 mAh g<sup>-1</sup> at 1.0 A g<sup>-1</sup>) was recorded in this work. Considering the prominent electrochemical performance of  $\alpha/h$ -MoO<sub>3</sub> homojunctions, in situ construction crystal phase homojunctions strategy on polymorph materials provides an alternative solution to the energy storage and related fields.

**Supplementary Materials:** The following supporting information can be downloaded at: <https://www.mdpi.com/article/10.3390/nano12213762/s1>, Figure S1: The first CV curves at 0.1 mV s<sup>-1</sup> of the electrodes. Figure S2: GCD curves at different current densities.

**Author Contributions:** D.H.L.N. and J.L. (Jiabiao Lian) conceived the idea and supervised the project. S.L., J.L. (Jun Li) and J.H. carried out the experiments and acquired the data. S.L. and Y.C. wrote the draft of the paper. D.H.L.N., J.L. (Jiabiao Lian) and C.W. proof read and revised the paper. All authors have read and agreed to the published version of the manuscript.

**Funding:** Financial support by the China Postdoctoral Science Foundation (2022M711381), National Natural Science Foundation of China (21706103), Nanjing Tech University Research Start-up Fund (38274017111), and Zhongyan Jilantai Chlor-Alkali Chemical Co., Ltd. (FZ2019-RWS-027) is gratefully acknowledged.

**Institutional Review Board Statement:** Not applicable.

**Informed Consent Statement:** Not applicable.

**Data Availability Statement:** Not applicable.

**Conflicts of Interest:** The authors declare no conflict of interest.

## References

1. Li, M.; Lu, J.; Chen, Z.; Amine, K. 30 Years of lithium-ion batteries. *Adv. Mater.* **2018**, *3*, 589–599. [[CrossRef](#)]
2. Xie, J.; Lu, Y.C. A Retrospective on lithium-ion batteries. *Nat. Commun.* **2020**, *11*, 2499. [[CrossRef](#)]
3. Tarascon, J.M.; Armand, M. Issues and challenges facing rechargeable lithium batteries. *Nature* **2001**, *414*, 359–367. [[CrossRef](#)]
4. Lu, Y.; Shin, K.H.; Yu, Y.; Hu, Y.; Liang, J.; Chen, K.; Yuan, H.; Park, H.S.; Wang, D. Multiple active sites carbonaceous anodes for Na<sup>+</sup> storage: Synthesis, electrochemical properties and reaction mechanism analysis. *Adv. Funct. Mater.* **2021**, *31*, 2007247. [[CrossRef](#)]
5. Fang, S.; Bresser, D.; Passerini, S. Transition metal oxide anodes for electrochemical energy storage in lithium- and sodium-ion batteries. *Adv. Energy Mater.* **2020**, *10*, 1902485. [[CrossRef](#)]
6. Jiang, Y.; Wang, Y.; Ni, J.; Li, L. Molybdenum-Based materials for sodium-ion batteries. *InfoMat* **2021**, *3*, 339–352. [[CrossRef](#)]
7. Xie, J.; Zhang, H.; Liu, Q.; Liu, X.; Lu, X. Recent progress of molybdenum-based materials in aqueous rechargeable batteries. *Mater. Today Adv.* **2020**, *8*, 100100. [[CrossRef](#)]
8. Chen, M.; Wang, Z.; Wang, Y.; Li, Y.; Chen, Q. Sodium-Ion storage mechanisms and design strategies of Molybdenum-Based materials: A Review. *Appl. Mater. Today* **2021**, *23*, 100985. [[CrossRef](#)]
9. Hu, B.; Mai, L.; Chen, W.; Yang, F. From MoO<sub>3</sub> Nanobelts to MoO<sub>2</sub> nanorods: Structure transformation and electrical transport. *ACS Nano* **2009**, *3*, 478–482. [[CrossRef](#)] [[PubMed](#)]
10. Jung, Y.S.; Lee, S.; Ahn, D.; Dillon, A.C.; Lee, S.-H. Electrochemical reactivity of ball-milled MoO<sub>3–y</sub> as anode materials for lithium-ion batteries. *J. Power Sources* **2009**, *188*, 286–291. [[CrossRef](#)]
11. Yang, C.; Lua, H.; Li, C.; Wang, L.; Wang, H. Spatially-confined electrochemical reactions of MoO<sub>3</sub> nanobelts for reversible high capacity: Critical roles of glucose. *Chem. Eng. J.* **2018**, *337*, 1–9. [[CrossRef](#)]
12. Yang, C.; Liu, X.; Yang, Z.; Gu, L.; Yu, Y. Improvement of Lithium storage performance of Molybdenum Trioxide by a synergistic effect of surface coating and oxygen vacancies. *Adv. Mater. Interfaces* **2016**, *3*, 1600730.
13. Chen, J.S.; Cheah, Y.L.; Madhavi, S.; Lou, X.W. Fast synthesis of r-MoO<sub>3</sub> nanorods with controlled aspect ratios and their enhanced lithium storage capabilities. *J. Phys. Chem. C* **2010**, *114*, 8675–8678. [[CrossRef](#)]
14. Yan, Y.; Li, S.; Yuan, B.; Hu, R.; Yang, L.; Liu, J.; Liu, J.; Wang, Y.; Luo, Z.; Ying, H.; et al. Flowerlike Ti-doped MoO<sub>3</sub> conductive anode fabricated by a novel NiTi dealloying method: Greatly enhanced reversibility of the conversion and intercalation reaction. *ACS Appl. Mater. Interfaces* **2020**, *12*, 8240–8248. [[CrossRef](#)]
15. Sahu, S.R.; Rikka, V.R.; Haridoss, P.; Chatterjee, A.; Gopalan, R.; Prakash, R. A NOVEL α-MoO<sub>3</sub>/single-walled carbon nanohorns composite as high-performance anode material for fast-charging lithium-ion battery. *Adv. Energy Mater.* **2020**, *10*, 2001627. [[CrossRef](#)]
16. Zhou, X.; Gao, Y.; Lyu, L.-H.; Liang, Y.; Li, Z. General construction of molybdenum-based compounds embedded in flexible 3D interconnected porous carbon nanofibers with protective porous shell for high-performance lithium-ion battery. *Carbon* **2021**, *179*, 142–150. [[CrossRef](#)]
17. Xia, Q.; Zhao, H.; Du, Z.; Zeng, Z.; Gao, C.; Zhang, Z.; Du, X.; Kulka, A.; Swierczek, K. Facile synthesis of MoO<sub>3</sub>/carbon nanobelts as high-performance anode material for lithium ion batteries. *Electrochim. Acta* **2015**, *180*, 947–956. [[CrossRef](#)]
18. Jiang, Y.; Sun, M.; Ni, J.; Li, L. Ultrastable sodium storage in MoO<sub>3</sub> nanotube arrays enabled by surface phosphorylation. *ACS Appl. Mater. Interfaces* **2019**, *11*, 37761–37767. [[CrossRef](#)] [[PubMed](#)]
19. Liu, S.; Xu, C.; Yang, H.; Qian, G.; Hua, S.; Liu, J.; Zheng, X.; Lu, X. Atomic modulation triggering improved performance of MoO<sub>3</sub> nanobelts for fiber-shaped supercapacitors. *Small* **2020**, *16*, 1905778. [[CrossRef](#)]
20. Chen, Y.; Lai, Z.; Zhang, X.; Fan, Z.; He, Q.; Tan, C.; Zhang, H. Phase engineering of nanomaterials. *Nat. Rev. Chem.* **2020**, *4*, 243–256. [[CrossRef](#)]
21. Hao, J.N.; Zhang, J.; Xia, G.L.; Liu, Y.J.; Zheng, Y.; Zhang, W.C.; Tang, Y.B.; Pang, W.K.; Guo, Z.P. Heterostructure manipulation via in situ localized phase transformation for high-rate and highly durable lithium ion storage. *ACS Nano* **2018**, *12*, 10430–10438. [[CrossRef](#)] [[PubMed](#)]
22. Li, Y.; Zhang, J.; Chen, Q.; Xia, X.; Chen, M. Emerging of heterostructure materials in energy storage: A review. *Adv. Mater.* **2021**, *33*, 2100855. [[CrossRef](#)] [[PubMed](#)]
23. Li, H.; Zhou, X.; Zhai, W.; Lu, S.; Liang, J.; He, Z.; Long, H.; Xiong, T.; Sun, H.; He, Q.; et al. Phase Engineering of Nanomaterials for Clean Energy and Catalytic Applications. *Adv. Energy Mater.* **2020**, *10*, 2002019. [[CrossRef](#)]
24. Liang, G.; Wang, Y.; Huang, Z.; Mo, F.; Li, X.; Yang, Q.; Wang, D.; Li, H.; Chen, S.; Zhi, C. Initiating hexagonal MoO<sub>3</sub> for superb-stable and fast NH<sub>4</sub><sup>+</sup> storage based on hydrogen bond chemistry. *Adv. Mater.* **2020**, *32*, 1907802. [[CrossRef](#)] [[PubMed](#)]
25. Almodóva, P.; López, M.L.; Julio, R.-C.; Nappini, S.; Magnano, E.; José, M.G.-C.; Carlos, D.-G. Synthesis, characterization and electrochemical assessment of hexagonal molybdenum trioxide (h-MoO<sub>3</sub>) micro-composites with graphite, graphene and graphene oxide for lithium ion batteries. *Electrochim. Acta* **2021**, *365*, 137355. [[CrossRef](#)]

26. Leng, K.; Chen, Z.; Zhao, X.; Tang, W.; Tian, B.; Nai, C.; Zhou, W.; Loh, K.P. Phase-junction electrocatalysts towards enhanced hydrogen evolution reaction in alkaline media. *Angew. Chem. Int. Ed.* **2021**, *60*, 259–267.
27. Zheng, L.; Xu, Y.; Jin, D.; Xie, Y. Novel metastable hexagonal MoO<sub>3</sub> nanobelts: Synthesis, photochromic, and electrochromic properties. *Chem. Mater.* **2009**, *21*, 5681–5690. [[CrossRef](#)]
28. Shen, F.; Sun, Z.; Zhao, L.; Xia, Y.; Shao, Y.; Cai, J.; Li, S.; Lu, C.; Tong, X.; Zhao, Y.; et al. Triggering the phase transition and capacity enhancement of Nb<sub>2</sub>O<sub>5</sub> for fast-charging lithium ion storage. *J. Mater. Chem. A* **2021**, *9*, 14534. [[CrossRef](#)]
29. Li, X.; Pan, D.; Deng, J.; Wang, R.; Huang, J.; Lu, W.; Yao, T.; Wang, X.; Zhang, Y.; Xu, L.; et al. Phase-junction engineering boosts the performance of CoSe<sub>2</sub> for efficient sodium/potassium storage. *J. Mater. Chem. A* **2021**, *9*, 25954–25963. [[CrossRef](#)]
30. Lunk, H.-J.; Hartl, H.; Hartl, M.A.; Fait, M.J.G.; Shenderovich, I.G.; Feist, M.; Frisk, T.A.; Daemen, L.L.; Mauder, D.; Eckelt, R.; et al. “Hexagonal Molybdenum Trioxide”; Known for 100 years and still a fount of new discoveries. *Inorg. Chem.* **2010**, *49*, 9400–9408. [[CrossRef](#)]
31. Ding, J.; Abbas, S.A.; Hanmandlu, C.; Lin, L.; Lai, C.-S.; Wang, P.-C.; Li, L.-J.; Chu, C.-W.; Chang, C.-C. Facile synthesis of carbon/MoO<sub>3</sub> nanocomposites as stable battery anodes. *J. Power Sources* **2017**, *348*, 270–280. [[CrossRef](#)]
32. Li, S.; Cui, Y.; Kang, R.; Zou, B.; Ng, D.H.L.; El-Khodary, S.A.; Liu, X.; Qiu, J.; Lian, J.; Li, H. Oxygen vacancies boosted the electrochemical kinetics of Nb<sub>2</sub>O<sub>5-x</sub> for superior lithium storage. *Chem. Commun.* **2021**, *57*, 8182–8185. [[CrossRef](#)] [[PubMed](#)]
33. Zou, B.; Zhang, W.; Cui, Y.; Li, S.; Li, G.; Liu, X.; Ng, D.H.L.; Qiu, J.; Lian, J. Interfacial engineering for metal oxides/nitrides nano-heterojunctions towards high-rate lithium-ion storage. *J. Mater. Chem. A* **2022**, *10*, 7391–7398. [[CrossRef](#)]
34. Zheng, Y.; Zhou, T.; Zhang, C.; Mao, J.; Liu, H.; Guo, Z. Boosted charge transfer in SnS/SnO<sub>2</sub> heterostructures: Toward high rate capability for sodium-ion batteries. *Angew. Chem. Int. Ed.* **2016**, *55*, 3408–3413. [[CrossRef](#)] [[PubMed](#)]
35. John, W.; Polleux, J.; Lim, J.; Dunn, B. Pseudocapacitive contributions to electrochemical energy storage in TiO<sub>2</sub> (Anatase) nanoparticles. *J. Phys. Chem. C* **2007**, *111*, 14925–14931.